batteries

MDPI

Article

Transition Metal-Based Polyoxometalates for Oxygen Electrode Bifunctional Electrocatalysis

Jadranka Milikić [1,†], Filipe Gusmão [2,†], Sara Knežević [3], Nemanja Gavrilov [1], Anup Paul [4], Diogo M. F. Santos [2] and Biljana Šljukić [2,*]

[1] Faculty of Physical Chemistry, University of Belgrade, Studentski trg 12–16, 11158 Belgrade, Serbia; jadranka@ffh.bg.ac.rs (J.M.); gavrilov@ffh.bg.ac.rs (N.G.)
[2] Center of Physics and Engineering of Advanced Materials, Laboratory for Physics of Materials and Emerging Technologies, Chemical Engineering Department, Instituto Superior Técnico, Universidade de Lisboa, 1049-001 Lisbon, Portugal; filipe.gusmao@tecnico.ulisboa.pt (F.G.); diogosantos@tecnico.ulisboa.pt (D.M.F.S.)
[3] CNRS, Bordeaux INP, Institut des Sciences Moléculaires, University of Bordeaux, UMR 5255, 33607 Pessac, France; sara.knezevic@u-bordeaux.fr
[4] Centro de Química Estrutural, Institute of Molecular Sciences, Instituto Superior Técnico, Universidade de Lisboa, Av. Rovisco Pais, 1049-001 Lisboa, Portugal; anuppaul@tecnico.ulisboa.pt
* Correspondence: biljana.paunkovic@tecnico.ulisboa.pt
† These authors contributed equally to this work.

Abstract: Polyoxometalates (POMs) with transition metals (Co, Cu, Fe, Mn, Ni) of Keggin structure and lamellar-stacked multi-layer morphology were synthesized. They were subsequently explored as bifunctional electrocatalysts for oxygen electrodes, i.e., oxygen reduction (ORR) and evolution (OER) reaction, for aqueous rechargeable metal-air batteries in alkaline media. The lowest Tafel slope (85 mV dec^{-1}) value and the highest OER current density of 93.8 mA cm^{-2} were obtained for the Fe-POM electrocatalyst. Similar OER electrochemical catalytic activity was noticed for the Co-POM electrocatalyst. This behavior was confirmed by electrochemical impedance spectroscopy, where Fe-POM gave the lowest charge transfer resistance of 3.35 Ω, followed by Co-POM with R_{ct} of 15.04 Ω, during the OER. Additionally, Tafel slope values of 85 and 109 mV dec^{-1} were calculated for Fe-POM and Co-POM, respectively, during the ORR. The ORR at Fe-POM proceeded by mixed two- and four-electron pathways, while ORR at Co-POM proceeded exclusively by the four-electron pathway. Finally, capacitance studies were conducted on the synthesized POMs.

Keywords: transition metals; polyoxometalates; oxygen reduction reaction; oxygen evolution reaction

check for updates

Citation: Milikić, J.; Gusmão, F.; Knežević, S.; Gavrilov, N.; Paul, A.; Santos, D.M.F.; Šljukić, B. Transition Metal-Based Polyoxometalates for Oxygen Electrode Bifunctional Electrocatalysis. *Batteries* **2024**, *10*, 197. https://doi.org/10.3390/batteries10060197

Academic Editor: Chunwen Sun

Received: 24 April 2024
Revised: 23 May 2024
Accepted: 28 May 2024
Published: 3 June 2024

Copyright: © 2024 by the authors. Licensee MDPI, Basel, Switzerland. This article is an open access article distributed under the terms and conditions of the Creative Commons Attribution (CC BY) license (https://creativecommons.org/licenses/by/4.0/).

1. Introduction

Ongoing energy crises and rising CO_2 emissions have highlighted the importance and urgency of transitioning from a fossil-fuels-based economy to one powered by cleaner, low- or no-carbon sources. However, the intermittent nature of renewable power sources (wind or solar energy) causes energy production to fluctuate over time, limiting their applicability and requiring eco-friendly energy storage devices.

Rechargeable aqueous metal–air batteries are sustainable and low-cost energy storage devices, manifesting high energy density and good ionic conductivity [1,2]. Nevertheless, their limitation lies in the sluggish kinetics and high overpotentials of the air electrode during discharge (oxygen reduction reaction, ORR) and charging (oxygen evolution reaction, OER) processes [2–6]. Being multistep electron transfer reactions, ORR and OER highly depend on the electrode material, with Pt/C being the most active electrocatalyst for ORR [3,4] and IrO_2 and RuO_2 for OER [5,6]. However, the limited stability, scarcity, and high price of these materials and the fact that they cannot efficiently catalyze both charging and discharge reactions encourage the development of new electrode materials for rechargeable metal-air batteries.

Polyoxometalates (POMs) are polyatomic transition metal oxyanions with a tridimensional framework, emerging as promising electrocatalysts owing to their high thermal stability, tunable structure, and mechanical and redox properties [7,8]. Thus, they have found applications as electrocatalysts for ORR [9–12] and OER [11,13–15] in fuel cells, batteries [9,11,13,16], and electrolytic cells [14]. Adjusting the electrochemical and mechanical properties of POMs can be accomplished by varying the composition of their framework by introducing different metal redox centers [17,18] or incorporating the whole POM structure into porous materials or conductive substrates [7]. Moreover, the effect of intrinsic structure adjustment in terms of anion structure regulation on POM electrocatalytic activity has been explored [19]. Anionic structure regulation led not only to the increased number of catalytically active sites, but further enhanced the catalytic site activity due to the enhancement of TM–oxygen covalence. Thus, the choice of an appropriate method for POM synthesis governs the physicochemical properties of a material (composition, surface area, porosity, etc.) and, consequently, electrochemical behavior in surface reactions at the electrolyte/electrode interface [19,20]. Adjustment of the porosity improves the contact between active sites and reactants, further enhancing POM electrocatalytic performance.

This work assessed the catalytic properties of Keggin-structure POMs with transition metal centers (Fe, Co, Cu, Mn, and Ni) toward ORR and OER (Scheme 1). The aim was to identify the most efficient lower-cost bifunctional catalysts for these reactions and understand the influence of the metal center on the structure-function properties of this POM family. These will enable the development of a rational design for POM-based electrocatalytic materials. Prepared TM-POMs were characterized by X-ray diffraction (XRD) analysis, scanning electron microscopy with integrated energy-dispersive X-ray spectroscopy (SEM-EDS) and transmission electron microscopy (TEM), and, finally, nitrogen sorption analysis. Electrochemical performance was run using voltammetry and electrochemical impedance spectroscopy (EIS).

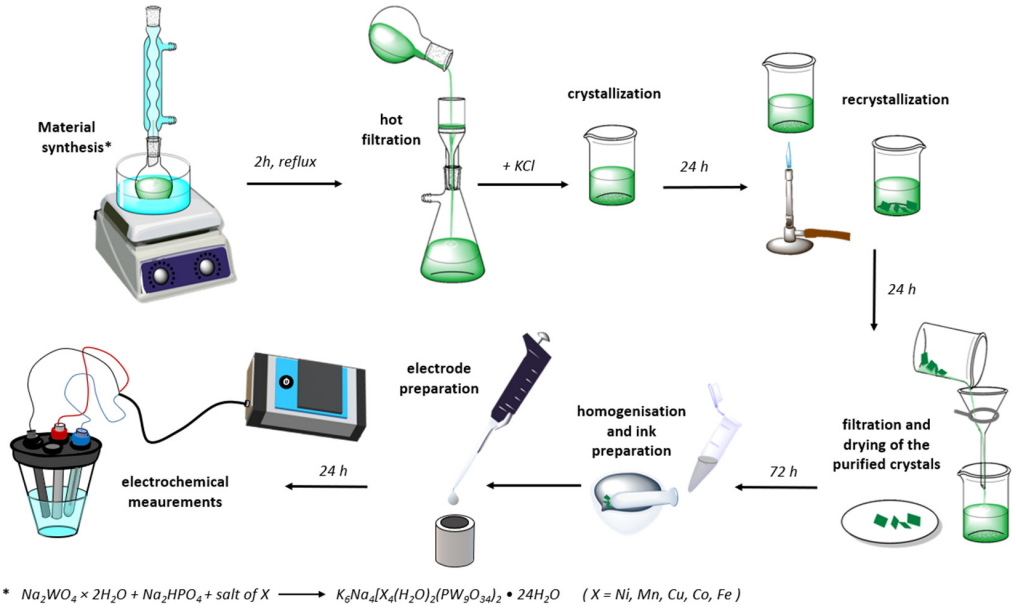

Scheme 1. Illustration of synthesis procedure of TM-POM and test apparatus.

2. Materials and Methods

2.1. Synthesis and Characterization of Five POMs Electrocatalysts

$K_6Na_4[X_4(H_2O)_2(PW_9O_{34})_2]\cdot 24H_2O$ POMs, where X = Ni, Mn, Cu, Co, and Fe were synthesized using a procedure similar to the one proposed by Clemente-Juan et al. [21]. Firstly, five 22 mM solutions were prepared by dissolving $MnSO_4\cdot H_2O$, $NiSO_4\cdot 6H_2O$, $(NH_4)_2Fe(SO_4)_2\cdot 6H_2O$, $CoSO_4$, and $CuSO_4\cdot 5H_2O$ in 5 mL of deionized water each. Secondly, 50 mL of a solution containing 0.1 M $Na_2WO_4\cdot 2H_2O$ and 11 mM Na_2HPO_4 was

vigorously stirred with a magnetic stirrer for 5 min, while the pH of the obtained solution was adjusted to 7 with the concentrated acetic acid. Finally, the prepared solutions of transition metal ions were added to 10 mL of tungstate solution each, and the obtained mixtures were refluxed for 2 h and then hot-filtered. A 0.4 g quantity of KCl was added to the hot filtrate, and the solution was left to crystalize overnight. The crystals were subsequently separated from the solution by filtration, redispersed in deionized water, and heated until dissolved. The following day, the recrystallized products were obtained by decanting excess solution and air-drying at room temperature.

Their structures were determined by XRD analysis using a Rigaku Ultima IV diffractometer in Bragg–Brentano geometry with Ni-filtered CuKα radiation (λ = 1.54178 Å). Moreover, Fourier transform infrared (FTIR) spectroscopy analysis was performed using a Perkin Elmer GX1 spectrometer. Scanning electron microscope Phenom™ ProX Desktop SEM (ThermoFisher Scientific™, Waltham, MA, USA) with integrated EDS detector and TEM performed on a HITACHI H-8100 microscope (Microscopy and analytical imaging research resource core laboratory, Lawrence, Kansas)were used for a complete examination of surface morphology, microstructure, and atomic composition of five TM-POMs. The sorption parameters were determined by analyzing nitrogen sorption isotherms at a temperature of 77 K. The measurements were conducted using a Micromeritics ASAP 2060 Surface Area Analyzer (MicrotracBEL, Osaka, Japan), following prior degassing of the samples at 150 °C for 36 h.

2.2. Electrocatalysis with Transition Metal POMs

The activity of the prepared POMs for OER and ORR electrocatalysis was assessed using a three-electrode cell with a saturated calomel electrode (SCE) as the reference, a graphite rod as the counter electrode, and the TM-POM deposited on a glassy carbon rotating disk electrode (RDE) as working electrode. All potentials are converted and presented versus the reversible hydrogen reference electrode (RHE). All electrodes were placed in 1 M KOH (80 mL) as the supporting electrolyte. The measurements were taken using an ALS/DY2325 bipotentiostat (ALS Co., Osaka, Japan) and an Ivium V01107 Potentiostat/Galvanostat (Ivium Technologies, Eindhoven, The Netherlands).

For the catalytic ink preparation for OER/ORR and double-layer capacitance studies, a mixture of powdered TM-POM (5 mg), distilled water (600 µL), ethanol (400 µL, 96%), and Nafion™ (25 µL, 0.5 wt.%) was sonicated in an Emmi®—08ST sonicator, EMAG Technologies (Ann Arbor, MI, USA). The inks were pipetted onto the RDE (0.071 cm^2), leading to a catalyst loading of 0.137 mg cm^{-2}. For the capacitance study, a mixture was composed of TM-POM (5 mg), activated carbon (1.35 mg), ethanol (27.5 µL), and Nafion™ (7.3 µL, 5 wt.%).

For capacitance measurements and one of the ORR studies, the electrolyte was saturated with N_2 gas for 20 min before the experiments. The remaining ORR experiments were run in an O_2-saturated electrolyte. The rotation rate of the disc electrode was varied: 300, 600, 900, 1200, 1800, 2400, and 3600 rpm at a scan rate of 5 mV s^{-1}. Lastly, electrochemical impedance spectroscopy experiments were conducted in the frequency range from 100 kHz to 0.1 Hz at 1.868 V.

Two different electrolytes were used for capacitance measurements, namely, 3 M KOH as alkaline media and 1 M H_2SO_4 as acidic media. The voltammograms were run from 0.20 to 0.62 V for alkaline media and 0.25 to 0.95 V for acidic media, using increasing scan rates of 5, 10, 20, 50, 100, and 200 mV s^{-1}. Following these measurements, potential cycling was performed for the best material by running 1000 cycles in 3 M KOH and 1 M H_2SO_4 at 0.5 A g^{-1} and 0.25 A g^{-1}, respectively.

Finally, EIS was performed in acidic media for all TM-POMs at open circuit potential (OCP) to determine electrolyte and charge transfer resistance.

3. Results

3.1. Characterization of TM-POMs

SEM images, together with the EDS spectra of the five POM samples, are presented in Figure 1. Two segregated phases with nanowires and large agglomerate parts were noticed in SEM images of Ni-POM (Figure 1A), Mn-POM (Figure 1B), Fe-POM (Figure 1C), and Co-POM (Figure 1E) samples, while Cu-POM (Figure 1D) also showed the presence of spherical particles. EDS spectra of five POM samples confirmed the presence of elements of POMs combined with Ni, Mn, Fe, Co, and Cu in the corresponding POM (Figure 1F illustrates the case of Fe-POM).

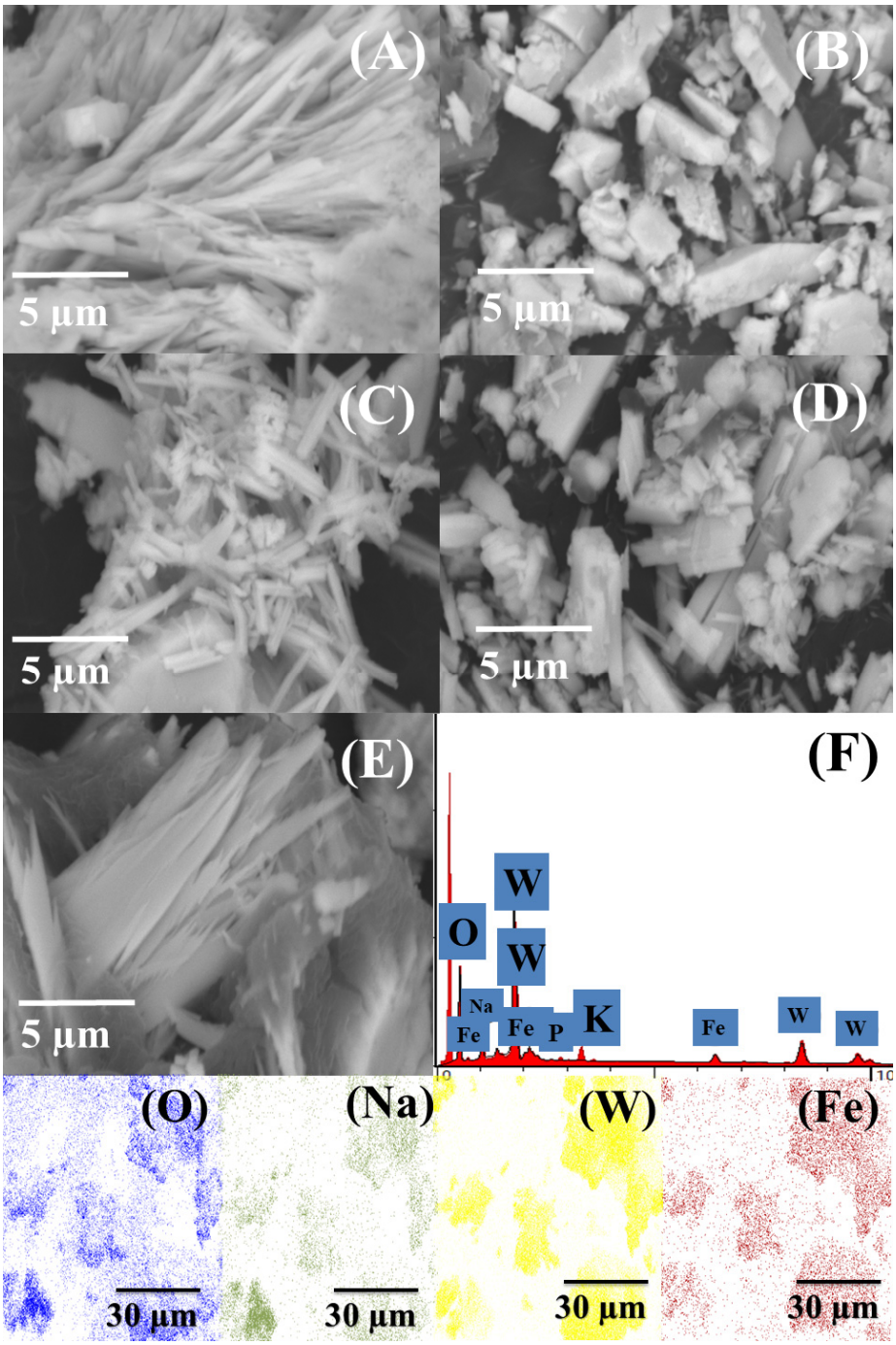

Figure 1. SEM images of (**A**) Ni-POM, (**B**) Mn-POM, (**C**) Fe-POM, (**D**) Cu-POM, and (**E**) Co-POM with (**F**) EDS spectrum and elemental mapping of Fe-POM.

TEM images of POM samples showed a mixed multi-layered structure of stacked lamellae obtained for Cu-POM, Co-POM, and Ni-POM (Figure 2A,C,E), and nanobelts for Mn-POM and Fe-POM (Figure 2B,D). Q. Liu et al. investigated cluster-assembled materials based on POMs and showed five different morphologies of Keggin POM-POSS Janus clusters in different solvent mixtures, confirmed by TEM analysis [22]. The morphology of obtained POMs [22] is similar to that of the POM materials synthesized herein.

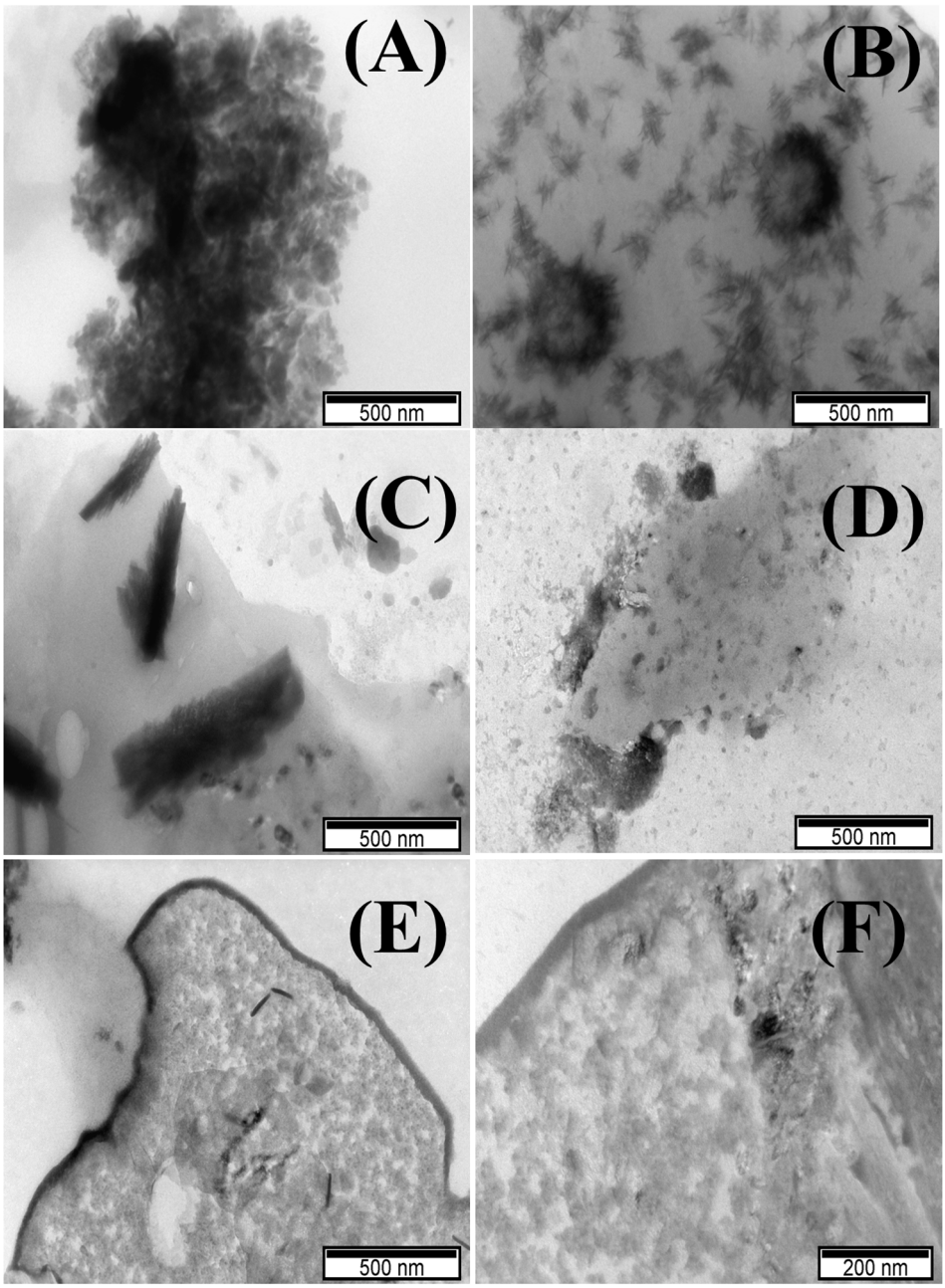

Figure 2. TEM images of (**A**) Cu-POM, (**B**) Mn-POM, (**C**) Co-POM, (**D**) Ni-POM, and (**E**,**F**) Fe-POM.

Figure 3A shows typical XRD patterns for the Keggin structure of five TM-POM samples [23–27]. The four characteristic peaks at 2θ of 25.02, 26.60, 37.5, and 42.01° were observed for all TM-POMs samples [24]. Lower peak intensities in the cases of Fe-POM and Ni-POM indicate lower crystallinity of their structures. Such structural disorder and the higher number of defects in nanomaterials of low crystallinity can give rise to higher electrochemical performance compared to their highly crystalline counterparts, as previously observed in the case of an electrocatalyst based on Fe_2O_3 [28] 10.3390/molecules28010434.

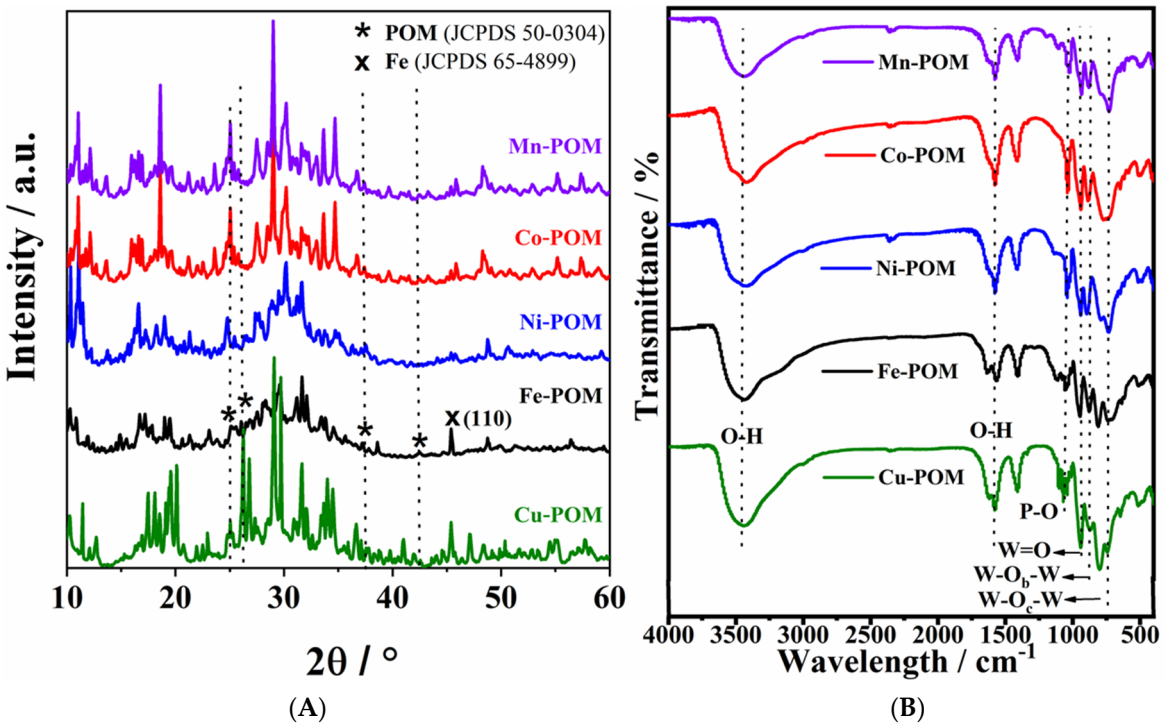

Figure 3. (**A**) XRD patterns and (**B**) FTIR spectra of five TM-POM electrocatalysts.

The FTIR spectra of the TM-POMs display bands characteristic of POMs in the 1100–740 cm^{-1} region (Figure 3B), thus confirming the POM structure. Namely, the bands at 1040, 945, 877, and 806 cm^{-1} correspond to the frequency of P-O in the central PO_4 and W=O in the exterior WO_6, W−O_b−W, and W−O_c−W bridges, respectively [29]. A characteristic shoulder in the P–O position results in a decreased symmetry of PO_4 tetrahedron. The bands at ~3490 and 1580 cm^{-1} are attributed to the stretching and banding vibration of the O–H bond within free H_2O molecules, respectively.

The surface area of POMs was investigated by conducting N_2 sorption measurements. The isotherms exhibited by all POMs were a combination of type I and IV, accompanied by H3 hysteresis loops. The resulting BET surface areas were approximately 3.2 m^2 g^{-1} for Co-POM, 1.9 m^2 g^{-1} for Cu-POM, 2.0 m^2 g^{-1} for Fe-POM, 1.0 m^2 g^{-1} for Mn-POM, and 3.0 m^2 g^{-1} for Ni-POM (Figure S1). To determine the pore size distribution (PSD), the nonlocal density functional theory (NLDFT) method was employed. Analysis of the PSD revealed distinct peaks for Co-, Cu-, Mn-, and Ni-POMs, indicating a significant concentration of mesopores within the size range of approximately 9–47 nm (Figure 4). However, in the case of Fe-POM, the PSD analysis exhibited peaks in the range of ca. 32–83 nm, indicating the presence of both mesopores and macropores (Figure 4C).

3.2. Catalysis of OER Using TM-POMs

TM-POMs were studied under OER polarization conditions in 1 M KOH electrolyte solution (Figure 5A). TM-POMs possess unique redox-active metal oxide clusters that can facilitate electron transfer processes, making them attractive candidates for electrocatalytic applications. Herein, Fe-POM showed the highest current density during OER (Equations (1)–(5)) of 93.8 mA cm^{-2}, followed by Co-POM with 43.1 mA cm^{-2} and Ni-POM with 11.8 mA cm^{-2}, while Cu-POM and Mn-POM were found to have a negligible current density at 2 V. Onset potential (E_{onset}), i.e., the potential to reach a current density of 1 mA cm^{-2}, was found to increase in the order Ni-POM (1.453 V) > Fe-POM (1.588 V) > Co-POM (1.683 V) > Cu-POM (1.948 V) > Mn-POM (1.966 V), Table 1. Fe-POM showed the lowest overpotential to reach a current density of 10 mA cm^{-2} (η_{10}) among the studied materials, with a value of 434 mV, i.e., 117 mV and 318 mV lower than that of Co-POM

(551 mV) and Ni-POM (752 mV), respectively, Table 1. Previously studied POM combined with poly(vinyl butyl imidazolium) cations and cobalt ([PVIM][V-Co_4]) showed an η_{10} of 430 mV in alkaline media, which is similar to the herein-obtained value for Fe-POM [30]. Ni-modified Keggin-type POM ($[PNi(H_2O)W_{11}O_{39}]^{5-}$) prepared with the zeolitic imidazolate framework ZIF 67 ($PNiW_{11}$@amZIF) and PW_{12}@amZIF examined for OER in 1 M KOH showed an η_{10} of 375 mV and 423 mV, respectively, which is somewhat lower/similar to the value obtained herein [31]. Cu-POM and Mn-POM did not reach a current density of 10 mA cm^{-2} within the studied potential range. Furthermore, the current density at an overpotential of 400 mV (j_{400}) was found to be the highest for Fe-POM and to decrease in the order Fe-POM (4.78 mA cm^{-2}) > Ni-POM (4.13 mA cm^{-2}) > Co-POM (0.14 mA cm^{-2}) > Cu-POM (0.04 mA cm^{-2}) > Mn-POM/rGO (0.03 mA cm^{-2}), Table 1.

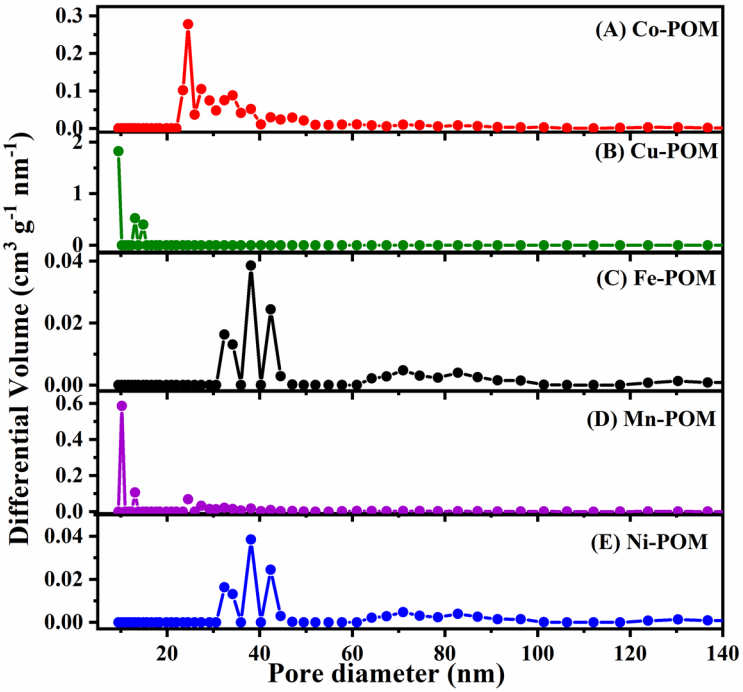

Figure 4. NLDFT pore size distribution curves of five TM-POM electrocatalysts: (**A**) Co-POM, (**B**) Cu-POM, (**C**) Fe-POM, (**D**) Mn-POM, and (**E**) Ni-POM.

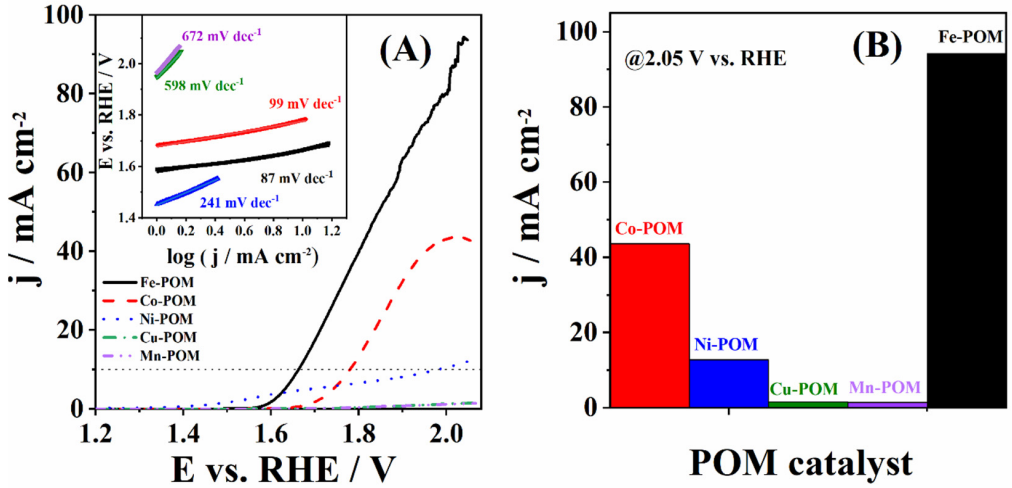

Figure 5. (**A**) LSVs (iR-corrected) of five TM-POMs in 1 M KOH with the corresponding Tafel plots (in inset) and (**B**) bar diagram presenting the highest OER current densities.

Table 1. Kinetic parameters for OER at TM-POMs compared with similar literature reports.

Catalyst	E_{onset}/V	η_{10}/mV	j_{400}/mA cm^{-2}	b/mV dec^{-1}	Source
Fe-POM	1.588	434	4.78	87	This work
Co-POM	1.683	551	0.14	99	This work
Ni-POM	1.453	752	4.13	241	This work
Cu-POM	1.948	–	0.04	598	This work
Mn-POM	1.966	–	0.03	672	This work
([PVIM][V-Co_4])	–	430	–	–	[30]
$PNiW_{11}$@amZIF	–	375	–	69	[31]
PW_{12}@amZIF	–	423	–	86	[31]
PW_{12}@FeOOH-P	–	230	–	79	[32]
PMo_{12}@FeOOH-P	–	235	–	123	[32]
SiW_{12}@FeOOH-P	–	260	–	126	[32]
FeOOH-P	–	290	–	202	[32]
CNCP-0	–	310	–	105.8	[33]
CNCP-1	–	293	–	88.2	[33]
CNCP-12	–	269	–	79.5	[33]
IrO_2	–	–	–	90.2	[33]
Fe_4@MWCNT_N6	–	580	–	102	[34]
NiP_4Mo_6	–	250	–	73	[9]

Tafel analysis was then performed to gain deeper insight into the electrocatalytic performance of the studied TM-POMs for OER, Figure 4B. The lowest Tafel slope (b) value of 87 mV dec^{-1} was determined for OER at Fe-POM. Co-POM (99 mV dec^{-1}) showed a somewhat higher Tafel slope value, while Ni-POM (241 mV dec^{-1}), Cu-POM (598 mV dec^{-1}), and Mn-POM (672 mV dec^{-1}) showed notably higher values, Table 1. Shang et al. [32] prepared different POM electrocatalysts, which were substituted with transition metal and mixed with β-FeOOH to obtain PW_{12}@FeOOH-P, PMo_{12}@FeOOH-P, SiW_{12}@FeOOH-P, and FeOOH-P. The lowest Tafel slope of 79 mV dec^{-1} was obtained for PW_{12}@FeOOH-P, and then somewhat higher values of 123 and 126 mV dec^{-1} were obtained for PMo_{12}@FeOOH-P and SiW_{12}@FeOOH-P, respectively. The highest Tafel value was calculated to be 202 mV dec^{-1} for the FeOOH-P electrocatalyst during OER. These results are comparable to those obtained for Fe-POM and Co-POM (Table 1). Different CNCP electrocatalyst nanoframes were prepared with a dodecahedral POM nanostructure and $[Co(CN)_6]^{3-}$ nanochannels and examined for OER in alkaline media [33]. CNCP-0, CNCP-1, CNCP-12, and IrO_2 showed Tafel slopes of 105.8, 88.2, 79.5, and 90.2 mV dec^{-1}, respectively. These values are comparable with the herein-determined values. Additionally, the best-performing material within this study, Fe-POM (87 mV dec^{-1}), has a Tafel slope comparable to or lower than those reported in the literature. For instance, Fe_4@MWCNT_N6 (102 mV dec^{-1}) electrocatalyst prepared with Fe-POMs compound and multi-walled carbon nanotubes [34] as well as NiP_4Mo_6 (73 mV dec^{-1}) synthesized with POM and appropriate Ni and Mo salts [9].

3.3. Catalysis of ORR Using TM-POMs

The performance of TM-POMs was next evaluated under ORR polarization conditions in 1 M KOH. A comparison of the current densities recorded in N_2- and O_2-saturated solutions shows an apparent increase in the presence of O_2 in the case of all TM-POMs, corresponding to oxygen reduction [35]. Figure 6A illustrates the case for Fe-POM (Figure S2 presents data for other TM-POMs). The most positive value of ORR peak potential (E_p) of 0.632 V was noticed for Fe-POM (Figure 6A), followed by 0.622, 0.558, 0.529, and 0.494 V recorded in the case of Mn-POM, Co-POM, Cu-POM, and Ni-POM, respectively. Herein, obtained peak potential values are in agreement with the literature reports [36–38]. All TM-POMs showed ORR peak current density of the same order of magnitude.

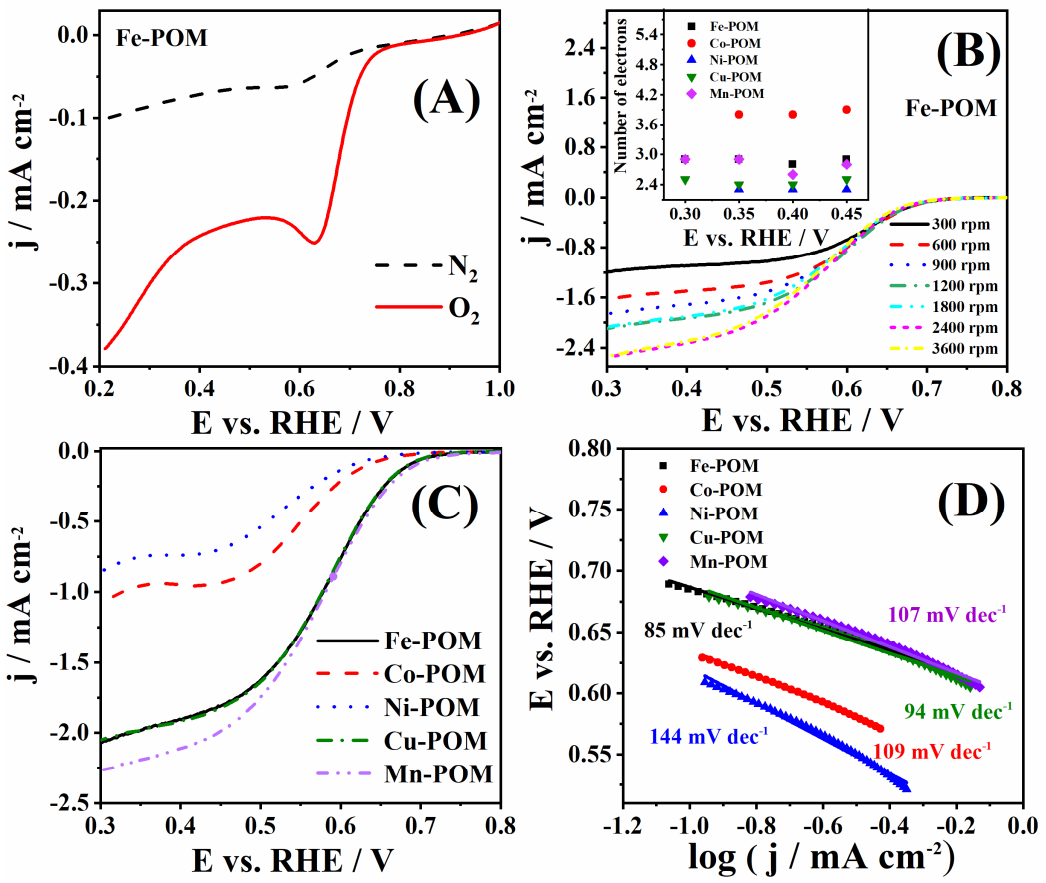

Figure 6. (**A**) Voltammograms of Fe-POM in N_2- and O_2-saturated 1 M KOH solution, (**B**) voltammograms of Fe-POM at different rotation rates with the number of electrons transferred for all five TM-POMs at different potentials in inset, and (**C**) voltammograms of five TM-POMs at 1800 rpm with (**D**) the corresponding Tafel plots.

RDE voltammograms of five TM-POMs collected at 1800 rpm are compared in Figure 6C. Mn-POM gave the highest ORR current density, followed by Fe-POM and Cu-POM, with somewhat lower ORR current densities. On the other hand, Ni-POM and Co-POM gave two times lower ORR current densities. Fe-POM, Cu-POM, and Mn-POM show slightly lower onset potential than Ni-POM and Co-POM (Table 2). Fe-POM and Cu-POM gave the most positive values of half-wave potential ($E_{1/2}$) of 0.580 V, whereas Co-POM and Mn-POM gave values lower for 28 and 24 mV, respectively. The lowest value of $E_{1/2}$ during ORR was found to be for the Ni-POM.

Figure 6C shows obtained Tafel plots and slopes (b) for five TM-POMs, where Fe-POM and Cu-POM offered the lowest values of 85 and 94 mV dec^{-1} (Table 2), Mn-POM and Co-POM gave a slightly higher value of 107 and 109 mV dec^{-1}, and finally Ni-POM showed the highest value of 144 mV dec^{-1}. Similar POM electrocatalysts, NiP_4Mo_6 and S-NiP_4Mo_6, presented Tafel slopes of 106 and 98 mV dec^{-1}, respectively [9]. Nanocomposite synthesized of phosphotungstate with carbon nanotubes doped with nitrogen ($Co_4(PW_9)_2$@N-CNT) led to an ORR Tafel slope 89 mV dec^{-1}, comparable with the herein-tested TM-POM electrocatalysts [39]. POM-like metal oxo clusters with molybdenum ($[Mo\text{-}oxo]_n$ clusters) synthesized on carbon showed a higher Tafel slope of 109 mV dec^{-1} during ORR [40].

Subsequently, voltammograms were recorded using different electrode rotation rates, Figure 6B and Figure S3. Koutecký–Levich analysis was performed using background-corrected data. The number of electrons (n) transferred during ORR was determined from the slope of Koutecký–Levich plots (j^{-1} vs. $\omega^{-1/2}$). ORR n values for Fe-POM were found to range from 2.8 to 2.9, Figure 6D, suggesting that the reduction of oxygen proceeds by both the two-electron pathway, where HO_2^- is formed as an intermediate

(Equations (6)–(8)), and four-electron pathway, where O_2 is directly reduced to OH^- (Equation (9)). n values for Cu-POM, Mn-POM, and Ni-POM were lower, suggesting a two-electron pathway. Similar results were reported for other POM electrodes [9,34,39,40]. The only exception was Co-POM with n values of 3.8–3.9 (Figure 6D), indicating that the process takes place exclusively through a four-electron pathway. $[PW_{11}MO_{39}]^{5-}$@Ru-rGO (M: Co, Ni, and Cu) electrocatalysts gave *n* between 3.9 and 4.2, which is comparable with the n value obtained for the herein-examined Co-POM electrocatalyst [41].

Table 2. Kinetic parameters of ORR for TM-POMs compared with similar literature reports.

Electrocatalysts	E_{onset}/V	$E_{1/2}$/V	E_{pp}/V	*b*/mV dec^{-1}	*n*	Source
Fe-POM	0.695	0.580	0.632	85	2.8–2.9	This work
Co-POM	0.655	0.552	0.558	109	3.8–3.9	This work
Ni-POM	0.639	0.533	0.494	144	2.3	This work
Cu-POM	0.695	0.580	0.529	94	2.4–2.5	This work
Mn-POM	0.694	0.556	0.622	107	2.6–2.9	This work
NiP_4Mo_6	–	–	–	106	3.80–3.85	[9]
S-NiP_4Mo_6	–	–	–	98	2.08–2.15	[9]
$Co_4(PW_9)_2$@N-CNT	0.90	–	–	89	2.73	[39]
$[Mo\text{-}oxo]_n$ clusters	0.75	–	0.62	109	~1.5	[40]
Fe_4@MWCNT_N6	0.81	–	–	35.4	2.9	[34]
Ni_4@MWCNT_N6	0.80	–	–	34.7	2.7	[34]
Fe_2Ni_2@MWCNT_N6	0.80	–	–	37.9	3.2	[34]
$[PW_{11}MO_{39}]_5$@Ru-rGO (M = Co, Ni, Cu)	–	–	–	–	3.9–4.2	[41]

The results obtained for OER/ORR catalysis by Fe-POM illustrate the importance of the electrocatalyst's electronic, structural, and morphological properties on its electrochemical performance. Fe's ability to undergo reversible redox reactions and the combination of catalytically active sites in high oxidation states with their easy accessibility due to a hierarchical porous structure and low crystallinity give rise to the high performance of Fe-POM for oxygen electrode reactions, mainly OER. Fe provides active adsorption sites capable of effectively binding oxygen species, thus modifying the Gibbs energy associated with oxygen adsorption as an important step in ORR.

3.4. Capacitance and Impedance Study

The electrocatalytic performance of materials for oxygen electrode reactions relies significantly on their pseudocapacitive characteristics, particularly oxygen adsorption (underpotential deposition) on the electrocatalyst's surface, which serves as a prerequisite for oxygen electrode processes. Enhanced pseudocapacitive behavior correlates with improved electrocatalytic performance, indicating a greater abundance of active sites available for participation in oxygen electrode processes. Characterization via cyclic voltammetry at various scan rates elucidates the rate capability of materials, reflecting their efficacy in adsorbing substantial amounts of oxygen and subsequently desorbing with high coulombic efficiency. Optimal pseudocapacitive behavior, manifested by the rectangular shape of CV curves, directly correlates with heightened electrocatalytic activity, as evidenced by lower overpotential values.

Double-layer capacitance (C_{dl}) values of studied TM-POMs (Figure S1) were found to be of the same order of magnitude, though higher in the case of Co-POM (400 μF cm^{-2}) compared to the other four TM-POMs (100–200 μF cm^{-2}). These values further suggest a similar electrochemically active surface area with active sites at the solid/electrolyte interface [35]. Thus, the difference in the TM-POMs' electrochemical response suggests different reactivity of the available catalytically active sites for the studied oxygen electrode reactions among five TM-POMs. The oxidation state and accessibility of active sites, along with other factors like charge transfer resistance, might play a role.

The charge storage behavior of five materials was further scrutinized in both alkaline (3 M KOH) and acidic (1 M H_2SO_4) media; Figure 7A,B illustrate the case of Co-POM, and Figure S4A,B illustrate a comparison of five TM-POMs' behavior at a common potential scan rate of 20 mV s^{-1}. The shape of the voltammograms clearly indicates the pseudocapacitance behavior of the studied TM-POMs in both media. Namely, both acidity and alkalinity in the electrolyte solution clearly activate faradaic processes in TM-POM surface atoms (at 0.75 V in 1 M H_2SO_4 and −1.12 V in 3 M KOH) that contribute to the charge storage capability of the materials' surface [42].

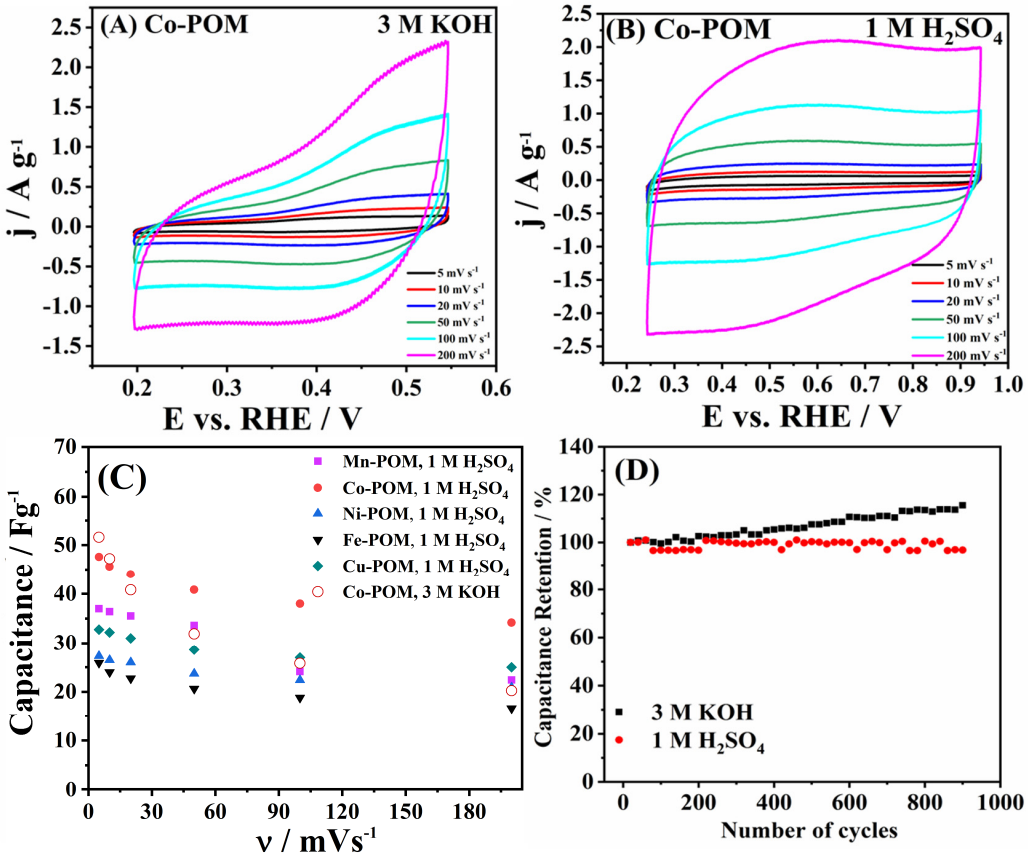

Figure 7. Capacitance study for Co-POM in (**A**) 3 M KOH and (**B**) 1 M H_2SO_4 at different scan rates. (**C**) Capacitance values of TM-POMs vs. scan rate and (**D**) cycling stability of Co-POM in 3 M KOH at 0.5 A g^{-1} and in 1 M H_2SO_4 at 0.25 A g^{-1}.

Specific capacitance (C_s) values of the same order of magnitude were determined for the five TM-POMs (Table S1) (in accordance with the similar specific surface areas), though they were higher in the case of Co-POM (47.6–34.2 F g^{-1}) versus other materials—Mn-POM (37.0–22.4 F g^{-1}), Cu-POM (32.8–25.0 F g^{-1}), Ni-POM (27.3–20.9 F g^{-1}), and Fe-POM (25.9–16.6 F g^{-1})—in acidic media. Furthermore, the capacitance values of the same order of magnitude were determined for two media, demonstrating that electrolyte solution composition does not notably affect the charge storage properties of TM-POM (Figure 7C, Table S1). The case of Co-POM that generally showed the highest values illustrates somewhat higher values of Co-POM in alkaline media compared to the acidic media at lower scan rates: capacitance of 51.6 and 47.2 F g^{-1} in 3 M KOH versus 47.6 and 45.6 F g^{-1} in 1 M H_2SO_4 at 5 and 10 mV s^{-1}, respectively. But at scan rate values of 20 mV s^{-1} and higher, the opposite becomes true, and capacitance values in H_2SO_4 become higher than in KOH with values ranging from 44.0 to 34.2 F g^{-1} versus 40.8 to 20.2 F g^{-1}.

Following this, continuous cycles were run in both media, with Figure 6D presenting specific capacitance values of Co-POM. Stable charge storage behavior could be observed

with a decrease of only 2.95% over 1000 cycles in 1 M H_2SO_4. Moreover, overall higher capacitance values were determined in the KOH solution, increasing over time to 115.5% of the initial values. This phenomenon can be attributed to the increase in electrolyte–electrode contact area, where running the measurement over a longer time allows for electrolyte ions to enter the material's pores [43].

EIS data of the five TM-POMs recorded at 1.868 V, i.e., in OER conditions, is presented in Figure 8A, which were fitted by the equivalent circuit given in the inset. Fe-POM gave the lowest charge transfer resistance (R_{ct}) of 3.35 Ω, followed by Co-POM, with a R_{ct} of 15.04 Ω (Table 3). Significantly higher R_{ct} values of 67.28, 137.0, and 239.0 Ω were observed for Cu-POM, Ni-POM, and Mn-POM electrocatalysts, respectively. These parameters agree with the OER kinetics parameters given in Table 1. These confirm the higher catalytic activity of Fe-POM and Co-POM towards OER compared to the rest of the TM-POMs.

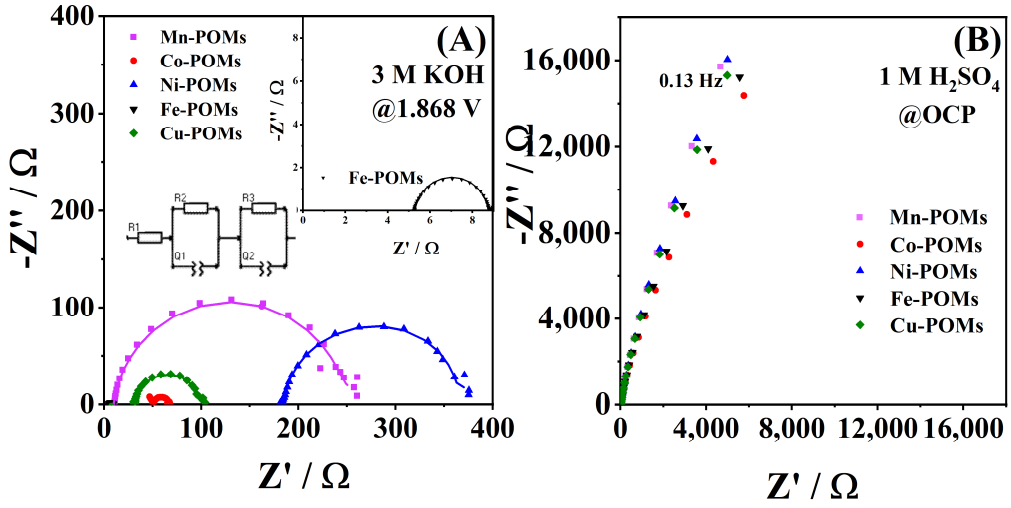

Figure 8. Nyquist plots of TM-POMs in (**A**) 1 M KOH at 1.868 V with the corresponding equivalent circuit used to fit the experimental data and with the high-frequency region in inset and (**B**) 1 M H_2SO_4 at OCP.

Table 3. EIS parameters of five TM-POMs in 1 M KOH at 1.868 V.

Electrocatalyst	R_s/Ω	R_e/Ω	R_{ct}/Ω	Q_e/mF	Q_{dl}/mF
Fe-POM	5.27	0.15	3.35	3.20×10^{-3}	7.40×10^{-4}
Co-POM	50.49	1.36	15.04	3.25×10^{-4}	1.93×10^{-2}
Ni-POM	184.80	44.78	137.00	8.08×10^{-4}	1.94×10^{-4}
Cu-POM	31.49	22.08	67.28	4.72×10^{-4}	6.57×10^{-4}
Mn-POM	9.25	2.68	239.00	8.22×10^{-2}	1.65×10^{-4}

R_s—electrolyte resistance; R_e—electronic resistance of the material and the associated capacitance; R_{ct}—charge transfer resistance; Q_e—constant phase element; Q_{dl}—ideal double-layer capacitor.

EIS was also run in 1 M H_2SO_4 at the OCP to evaluate the TM-POMs' resistance in acidic media. Figure 8B evidences a high impedance for the five TM-POMs. Frequency values, in inverse proportion with the relaxation time during which charge storage and transport take place (i.e., lower the frequency, longer the time for electrochemical phenomena to take place [43]), were found to be similar for the studied TM-POMs.

4. Discussion

Considering the kinetic parameters analyzed above (Tables 1 and 2), the optimum catalyst for OER can be determined. Fe-POM presented the lowest potential to reach the benchmark current density of 10 mA cm^{-2}, along with the lowest Tafel slope value and the highest OER current density of 93.8 mA cm^{-2}. Correspondingly, the current density at an overpotential of 400 mV delivered by Fe-POM was much higher than the other

four composites, leading to the conclusion that this material exhibits the optimum performance for OER among the five studied TM-POMs. This material performance is also comparable to other POMs reported in the literature, Table 1 [8].

The catalytic activity of Fe-POM in OER stems from its ability to undergo reversible redox reactions, providing active sites for the adsorption and activation of reactant molecules (Equations (1)–(5)) and facilitating the transfer of electrons during the reaction [44]. Fe-POM indeed showed the lowest charge transfer resistance value under OER conditions. Its mentioned lower crystallinity with accompanying structure disorder and presence of defects boost the oxygen electrode kinetics. Additionally, the presence of Fe in POM can play a crucial role in promoting specific catalytic pathways and improving overall catalytic efficiency. The herein-prepared Fe-POM has a hierarchical porous structure that combines the advantages of macro- and mesopores for improved kinetics [35]. Macropores present in Fe-POM contributed to the enhanced electrode kinetics by increasing the effective surface area accessible to the electrolyte and available for electrochemical reactions. Although the primary surface area contribution comes from mesopores (2–50 nm) and micropores (<2 nm), macropores facilitate the accessibility of these smaller pores by electrolyte ions. Furthermore, present macropores act as channels facilitating electrolyte ion movement to/from the surface active sites and thus reducing the ions' diffusion path length. By facilitating ion transport, macropores reduced the overall ionic resistance of Fe-POM. Finally, macropore presence is especially important in reactions involving gas evolution, such as the herein-studied OER improving gas management, i.e., allowing for generated gas bubbles to escape more easily, preventing the build-up of pressure, and ensuring the electrode surface remains accessible for the reaction.

$$M + OH^- \rightarrow MOH + e^- \quad (1)$$

$$MOH \rightarrow MO + H^+ + e^- \quad (2)$$

$$2MO \rightarrow 2M + O_{2(g)} \quad (3)$$

$$MO + H_2O \rightarrow MOOH + H^+ + e^- \quad (4)$$

$$MOOH \rightarrow M + O_{2(g)} + H^+ + e^- \quad (5)$$

$$\text{Sum reaction: } 4OH^- \rightarrow O_2 + 2H_2O + 4e^- \quad (6)$$

Regarding the lowest onset potential and Tafel slope, Fe-POM demonstrated the best ORR performance as well, followed by Co-POM. On the other hand, Ni-POM showed the lowest ORR performance with the highest Tafel slope and the lowest ORR current density. The reactivity of individual steps in an ORR is intricately linked to several factors, notably, the energy associated with oxygen adsorption, the dissociation energy of the O-O bond, and the binding affinity of hydroxide ions (OH^-) to the surface (Equations (7)–(10)).

$$O_{2,ads} + H_2O + 2e^- \rightarrow {HO_{2(ads)}}^- + OH^- \quad (7)$$

$${HO_{2(ads)}}^- + H_2O + 2e^- \rightarrow 3OH^- \quad (8)$$

$$2{HO_{2(ads)}}^- \rightarrow 2OH^- + O_2 \quad (9)$$

$$O_{2(ads)} + 2H_2O + 4e^- \rightarrow 4OH^- \quad (10)$$

Consequently, the heightened activity of Fe-POM in ORR may be attributed to its comparatively lower Gibbs free energy of oxygen adsorption, influenced by both geometric and electronic effects. Fe is posited to offer active adsorption sites capable of effectively binding oxygen species, thereby enhancing the overall adsorption capacity towards oxygen. Consequently, a plentiful presence of Fe sites on the catalyst surface can mitigate the Gibbs energy associated with oxygen adsorption during the initial step of the ORR.

5. Conclusions

Transition metal (Co, Cu, Fe, Mn, and Ni) polyoxometalates of the Keggin structure were synthesized and characterized by XRD, N_2-sorption, SEM-EDS, and TEM techniques. The bifunctional activity of TM-POMs for OER and ORR was evaluated in alkaline media. Fe-POM showed the best performances for both oxygen electrode reactions, followed by the Co-POM. Comparable Tafel slope values of 87 and 99 mV dec^{-1} were obtained for Fe-POM and Co-POM during OER, respectively. The rest of the TM-POM electrocatalysts showed substantially higher Tafel slopes in the range of 241 to 679 mV dec^{-1}. The OER current density at an overpotential of 400 mV delivered by Fe-POM was considerably higher than that of the other four POMs. Furthermore, Fe-POM showed the lowest onset potential and Tafel slope during ORR, and these values of Fe-POM were followed by the Co-POM. The ORR for Cu-POM, Mn-POM, and Ni-POM proceeded by the two-electron pathway, for Fe-POM by mixed two- and two-electron pathways, and for Co-POM by a four-electron pathway. Fe-POM's good performance arises from its ability to undergo reversible redox reactions along with its hierarchical porous structure and low crystallinity, i.e., easily accessible active sites with appropriate Gibbs free energy of oxygen species adsorption. The demonstrated activity of TM-POMs, specifically Fe-POM and Co-POM, for OER/ORR could be promising for their potential applications in rechargeable metal-air batteries and unitized regenerative fuel cells.

Supplementary Materials: The following supporting information can be downloaded at https://www.mdpi.com/article/10.3390/batteries10060197/s1, Figure S1: N2-adsorption–desorption isotherms of (a) Co-POM, (b) Cu-POM, (c) Fe-POM, (d) Mn-POM, and (f) Ni-POM.; Figure S2. Voltammograms of Fe-POM (A), Co-POM (B), Ni-POM (C), Cu-POM (D), and Mn-POM (E) in N2-saturated 1 M KOH solution at different scan rates (100 to 500 mV s−1) and corresponding double-layer capacitance plots (F).; Figure S3. Voltammograms of Co-POM (A), Ni-POM (B), Cu-POM (C), and Mn-POM (D) in N2- and O2-saturated 1 M KOH solution.; Figure S4. Voltammograms of Co-POM (A), Ni-POM (B), Cu-POM (C), and Mn-POM (D) at different rotation rates in O2-saturated 1 M KOH solution.; Figure S5. Voltammograms of TM-POMs at 20 mV s−1 (A) and of Co-POM (B), Cu-POM (C), Fe-POM (D), Ni-POM (E) and Mn-POM (F) at different scan rates in 1 M H2SO4.; Table S1: Specific capacitance of TM-POM in 3 M KOH and 1 M H_2SO_4.

Author Contributions: Conceptualization, B.Š.; formal analysis, J.M., F.G. and A.P.; investigation, J.M., F.G., S.K., N.G. and A.P.; writing—original draft preparation, J.M., F.G. and A.P.; writing—review and editing, D.M.F.S. and B.Š.; visualization, J.M., F.G. and A.P.; supervision, N.G., D.M.F.S. and B.Š.; project administration, B.Š.; funding acquisition, B.Š. All authors have read and agreed to the published version of the manuscript.

Funding: This research was funded by Fundação para a Ciência e a Tecnologia (FCT, Portugal), grant number EXPL/EQU-EQU/0517/2021. DMFS, BŠ, and AP were funded by FCT, contract no. UIDP/04540/2020, IST-ID/156-2018, and IST-ID/197/2019 (DOI: 10.54499/DL57/2016/CP1384/CT0081), respectively. This research was also funded by the Ministry of Science, Technological Development, and Innovation of the Republic of Serbia, grant numbers 451-03-65/2024-03/200146 and 451-03-66/2024-03/200146.

Data Availability Statement: Dataset available on request from the authors.

Conflicts of Interest: The authors declare no conflicts of interest.

References

1. Ling, W.; Wang, H.; Chen, Z.; Ji, Z.; Wang, J.; Wei, J.; Huang, Y. Intrinsic Structure Modification of Electrode Materials for Aqueous Metal-Ion and Metal-Air Batteries. *Adv. Funct. Mater.* **2021**, *31*, 2006855. [CrossRef]
2. Liu, Q.; Pan, Z.; Wang, E.; An, L.; Sun, G. Aqueous Metal-Air Batteries: Fundamentals and Applications. *Energy Storage Mater.* **2020**, *27*, 478–505. [CrossRef]
3. Zhang, J.; Yang, H.; Liu, B. Coordination Engineering of Single-Atom Catalysts for the Oxygen Reduction Reaction: A Review. *Adv. Energy Mater.* **2021**, *11*, 2002473. [CrossRef]
4. Zhou, W.; Su, H.; Cheng, W.; Li, Y.; Jiang, J.; Liu, M.; Yu, F.; Wang, W.; Wei, S.; Liu, Q. Regulating the Scaling Relationship for High Catalytic Kinetics and Selectivity of the Oxygen Reduction Reaction. *Nat. Commun.* **2022**, *13*, 6414. [CrossRef] [PubMed]

5. Xie, X.; Du, L.; Yan, L.; Park, S.; Qiu, Y.; Sokolowski, J.; Wang, W.; Shao, Y. Oxygen Evolution Reaction in Alkaline Environment: Material Challenges and Solutions. *Adv. Funct. Mater.* **2022**, *32*, 2110036. [CrossRef]
6. Chen, F.Y.; Wu, Z.Y.; Adler, Z.; Wang, H. Stability Challenges of Electrocatalytic Oxygen Evolution Reaction: From Mechanistic Understanding to Reactor Design. *Joule* **2021**, *5*, 1704–1731. [CrossRef]
7. Li, N.; Liu, J.; Dong, B.X.; Lan, Y.Q. Polyoxometalate-Based Compounds for Photo- and Electrocatalytic Applications. *Angew. Chem.-Int. Ed.* **2020**, *59*, 20779–20793. [CrossRef] [PubMed]
8. Gusmão, F.M.B.; Mladenović, D.; Radinović, K.; Santos, D.M.F.; Šljukić, B. Polyoxometalates as Electrocatalysts for Electrochemical Energy Conversion and Storage. *Energies* **2022**, *15*, 9021. [CrossRef]
9. Zheng, Y.; Xu, X.; Chen, J.; Wang, Q. Surface O^{2-} Regulation on POM Electrocatalyst to Achieve Accurate 2e/4e-ORR Control for H2O2 Production and Zn-Air Battery Assemble. *Appl. Catal. B* **2021**, *285*, 119788. [CrossRef]
10. Song, Y.; Peng, Y.; Yao, S.; Zhang, P.; Wang, Y.; Gu, J.; Lu, T.; Zhang, Z. Co-POM@MOF-Derivatives with Trace Cobalt Content for Highly Efficient Oxygen Reduction. *Chin. Chem. Lett.* **2022**, *33*, 1047–1050. [CrossRef]
11. Yin, D.; Wang, M.L.; Cao, Y.D.; Yang, X.; Ji, S.Y.; Hao, H.P.; Gao, G.G.; Fan, L.L.; Liu, H. Polyoxometalate@ZIF Induced CoWO4/WS2@C-N Nanoflower as a Highly Efficient Catalyst for Zn-Air Batteries. *ACS Appl. Energy Mater.* **2021**, *4*, 6892–6902. [CrossRef]
12. Nagaiah, T.C.; Gupta, D.; Das Adhikary, S.; Kafle, A.; Mandal, D. Tuning Polyoxometalate Composites with Carbonaceous Materials towards Oxygen Bifunctional Activity. *J. Mater. Chem. A Mater.* **2021**, *9*, 9228–9237. [CrossRef]
13. Yin, X.; Zhang, Z.; Yao, K.; Xu, X.; Wang, Y. Hydrophobic POM Electrocatalyst Achieves Low Voltage "Charge" in Zn-Air Battery Coupled with Bisphenol A Degradation. *Chemistry* **2021**, *27*, 8774–8781. [CrossRef] [PubMed]
14. Liu, Z.; Yuan, L.; Wen, T.; Yu, J.; Xu, X. Enhanced Electrocatalytic Activity of POM-Derived CoMoS/FCP Heterostructures for Overall Water Splitting in Alkaline Media. *Int. J. Electrochem. Sci.* **2023**, *18*, 100076. [CrossRef]
15. Gautam, J.; Kannan, K.; Meshesha, M.M.; Dahal, B.; Subedi, S.; Ni, L.; Wei, Y.; Yang, B.L. Heterostructure of Polyoxometalate/Zinc-Iron-Oxide Nanoplates as an Outstanding Bifunctional Electrocatalyst for the Hydrogen and Oxygen Evolution Reaction. *J. Colloid. Interface Sci.* **2022**, *618*, 419–430. [CrossRef] [PubMed]
16. Huang, B.; Yang, D.H.; Han, B.H. Application of Polyoxometalate Derivatives in Rechargeable Batteries. *J. Mater. Chem. A Mater.* **2020**, *8*, 4593–4628. [CrossRef]
17. Singh, G.; Das Adhikary, S.; Mandal, D. Physico- and Electrochemical Properties of First-Row Transition-Metal-Substituted Sandwich Polyoxometalates. *Inorg. Chem.* **2023**, *62*, 8551–8564. [CrossRef] [PubMed]
18. Mir, S.; Yadollahi, B.; Omidyan, R. Theoretical Comparative Survey on the Structure and Electronic Properties of First Row Transition Metal Substituted Keggin Type Polyoxometalates. *J. Solid. State Chem.* **2022**, *305*, 122667. [CrossRef]
19. Wang, Y.; Li, L.; Wang, S.; Dong, X.; Ding, C.; Mu, Y.; Cui, M.; Hu, T.; Meng, C.; Zhang, Y. Anion Structure Regulation of Cobalt Silicate Hydroxide Endowing Boosted Oxygen Evolution Reaction. *Small* **2024**. [CrossRef]
20. Mu, Y.; Wang, T.; Zhang, J.; Meng, C.; Zhang, Y.; Kou, Z. Single-Atom Catalysts: Advances and Challenges in Metal-Support Interactions for Enhanced Electrocatalysis. *Electrochem. Energy Rev.* **2022**, *5*, 145–186. [CrossRef]
21. Clemente-Juan, J.M.; Coronado, E.; Galán-Mascarós, J.R.; Gómez-García, C.J.G. Increasing the Nuclearity of Magnetic Polyoxometalates. Syntheses, Structures, and Magnetic Properties of Salts of the Heteropoly Complexes $[Ni_3(H_2O)_3(PW_{10}O_{39})H_2O]^{7-}$, $[Ni_4(H_2O)_2(PW_9O_{34})_2]^{10-}$, and $[Ni_9(OH)_3(H_2O)_6(HPO_4)_2(PW_9O_{34})_3]^{16-}$. *Inorg. Chem.* **1999**, *38*, 55–63. [CrossRef]
22. Liu, Q.; Wang, X. Polyoxometalate Clusters: Sub-Nanometer Building Blocks for Construction of Advanced Materials. *Matter* **2020**, *2*, 816–841. [CrossRef]
23. Lafuente, M.; Pellejero, I.; Clemente, A.; Urbiztondo, M.A.; Mallada, R.; Reinoso, S.; Pina, M.P.; Gandía, L.M. In Situ Synthesis of SERS-Active Au@POM Nanostructures in a Microfluidic Device for Real-Time Detection of Water Pollutants. *ACS Appl. Mater. Interfaces* **2020**, *12*, 36458–36467. [CrossRef] [PubMed]
24. Yokuş, Ö.A.; Kardaş, F.; Akyildirim, O.; Eren, T.; Atar, N.; Yola, M.L. Sensitive Voltammetric Sensor Based on Polyoxometalate/Reduced Graphene Oxide Nanomaterial: Application to the Simultaneous Determination of l-Tyrosine and l-Tryptophan. *Sens. Actuators B Chem.* **2016**, *233*, 47–54. [CrossRef]
25. Rajkumar, T.; Rao, G.R. Investigation of Hybrid Molecular Material Prepared by Ionic Liquid and Polyoxometalate Anion. *J. Chem. Sci.* **2008**, *120*, 587–594. [CrossRef]
26. Karimi, Z.; Mahjoub, A.R.; Harati, S.M. Polyoxometalate-Based Hybrid Mesostructured Catalysts for Green Epoxidation of Olefins. *Inorg. Chim. Acta* **2011**, *376*, 1–9. [CrossRef]
27. Cuentas-Gallegos, A.K.; Martínez-Rosales, R.; Rincón, M.E.; Hirata, G.A.; Orozco, G. Design of Hybrid Materials Based on Carbon Nanotubes and Polyoxometalates. *Opt. Mater.* **2006**, *29*, 126–133. [CrossRef]
28. Wu, C.; Pei, Z.; Lv, M.; Huang, D.; Wang, Y.; Yuan, S. Polypyrrole-Coated Low-Crystallinity Iron Oxide Grown on Carbon Cloth Enabling Enhanced Electrochemical Supercapacitor Performance. *Molecules* **2023**, *28*, 434. [CrossRef] [PubMed]
29. Tarlani, A.; Abedini, M.; Nemati, A.; Khabaz, M.; Amini, M.M. Immobilization of Keggin and Preyssler Tungsten Heteropolyacids on Various Functionalized Silica. *J. Colloid. Interface Sci.* **2006**, *303*, 32–38. [CrossRef]
30. Singh, G.; Adhikary, S.D.; Mandal, D. Stabilization and Activation of Polyoxometalate over Poly(Vinyl Butylimidazolium) Cations towards Electrocatalytic Water Oxidation in Alkaline Media. *Chem. Commun.* **2023**, *59*, 4774–4777. [CrossRef]
31. Zhao, Y.; Gao, D.; Biskupek, J.; Kaiser, U.; Liu, R.; Streb, C. Polyoxometalate-Assisted Synthesis of Amorphous Zeolitic Imidazolate for Efficient Electrocatalytic Oxygen Evolution. *Results Chem.* **2022**, *4*, 100568. [CrossRef]

32. Shang, W.; Wang, Y.; Jiang, Y.; Wu, M.; Zeng, M.; Wang, P.; Qiu, L.; Jia, Z. Nanocomposite: Co4-Substituted Polyoxometalate@β-FeOOH as High-Performance Electrocatalysts for Oxygen Evolution Reaction in Alkaline Conditions. *Appl. Catal. A Gen.* **2022**, *644*, 118810. [CrossRef]
33. Kang, Q.; Lai, D.; Su, M.; Xiong, B.; Tang, W.; Lu, Q.; Gao, F. Tailored Dodecahedral Polyoxometalates Nanoframes with in Situ Encapsulated Co, N, C for Oxygen Evolution Reaction. *Chem. Eng. J.* **2022**, *430*, 133116. [CrossRef]
34. Marques, I.S.; Jarrais, B.; Mbomekallé, S.M.; Teillout, A.L.; De Oliveira, P.; Freire, C.; Fernandes, D.M. Synergetic Effects of Mixed-Metal Polyoxometalates@Carbon-Based Composites as Electrocatalysts for the Oxygen Reduction and the Oxygen Evolution Reactions. *Catalysts* **2022**, *12*, 440. [CrossRef]
35. Mladenović, D.; Daş, E.; Santos, D.M.F.; Yurtcan, A.B.; Miljanić, Š.; Šljukić, B. Boosting Oxygen Electrode Kinetics by Addition of Cost-Effective Transition Metals (Ni, Fe, Cu) to Platinum on Graphene Nanoplatelets. *J. Alloys Compd.* **2022**, *905*, 164156. [CrossRef]
36. Milikić, J.; Stojanović, S.; Damjanović-Vasilić, L.; Vasilić, R.; Šljukić, B. Efficient Bifunctional Cerium-Zeolite Electrocatalysts for Oxygen Evolution and Oxygen Reduction Reactions in Alkaline Media. *Synth. Met.* **2023**, *292*, 117231. [CrossRef]
37. Milikić, J.; Knežević, S.; Stojadinović, S.; Alsaiari, M.; Harraz, F.A.; Santos, D.M.F.; Šljukić, B. Facile Synthesis of Low-Cost Copper-Silver and Cobalt-Silver Alloy Nanoparticles on Reduced Graphene Oxide as Efficient Electrocatalysts for Oxygen Reduction Reaction in Alkaline Media. *Nanomaterials* **2022**, *12*, 2657. [CrossRef] [PubMed]
38. Milikić, J.; Knežević, S.; Ognjanović, M.; Stanković, D.; Rakočević, L.; Šljukić, B. Template-Based Synthesis of Co3O4 and Co3O4/SnO2 Bifunctional Catalysts with Enhanced Electrocatalytic Properties for Reversible Oxygen Evolution and Reduction Reaction. *Int. J. Hydrogen Energy* **2023**, *48*, 27568–27581. [CrossRef]
39. Fernandes, D.M.; Novais, H.C.; Bacsa, R.; Serp, P.; Bachiller-Baeza, B.; Rodríguez-Ramos, I.; Guerrero-Ruiz, A.; Freire, C. Polyoxotungstate@Carbon Nanocomposites As Oxygen Reduction Reaction (ORR) Electrocatalysts. *Langmuir* **2018**, *34*, 6376–6387. [CrossRef]
40. Liu, R.; Cao, K.; Clark, A.H.; Lu, P.; Anjass, M.; Biskupek, J.; Kaiser, U.; Zhang, G.; Streb, C. Top-down Synthesis of Polyoxometalate-like Sub-Nanometer Molybdenum-Oxo Clusters as High-Performance Electrocatalysts. *Chem. Sci.* **2020**, *11*, 1043–1051. [CrossRef]
41. Ensafi, A.A.; Heydari-Soureshjani, E.; Rezaei, B. [PW11MO39]5− Decorated on Ru-Reduced Graphene Oxide Nanosheets, Characterizations and Application as a High Performance Storage Energy and Oxygen Reduction Reaction. *Chem. Eng. J.* **2017**, *330*, 1109–1118. [CrossRef]
42. Gezović, A.; Mišurović, J.; Milovanović, B.; Etinski, M.; Krstić, J.; Grudić, V.; Dominko, R.; Mentus, S.; Vujković, M.J. High Al-Ion Storage of Vine Shoots-Derived Activated Carbon: New Concept for Affordable and Sustainable Supercapacitors. *J. Power Sources* **2022**, *538*, 231561. [CrossRef]
43. Gandara, M.; Mladenović, D.; Oliveira Martins, M.d.J.; Rakocevic, L.; Kruszynski de Assis, J.M.; Šljukić, B.; Sarmento Gonçalves, E. MAX Phase (Nb_4AlC_3) For Electrocatalysis Applications. *Small* **2024**. [CrossRef] [PubMed]
44. Milikić, J.; Nastasić, A.; Rakočević, L.; Radinović, K.; Stojadinović, S.; Stanković, D.; Šljukić, B. FeM/RGO (M = Ni and Cu) as Bifunctional Oxygen Electrode. *Fuel* **2024**, *368*, 131654. [CrossRef]

Disclaimer/Publisher's Note: The statements, opinions and data contained in all publications are solely those of the individual author(s) and contributor(s) and not of MDPI and/or the editor(s). MDPI and/or the editor(s) disclaim responsibility for any injury to people or property resulting from any ideas, methods, instructions or products referred to in the content.